POLITECNICO DI TORINO
Repository ISTITUZIONALE

A novel approach to the study of magnetohydrodynamic effect on tritium transport in WCLL breeding blanket of DEMO

(Article begins on next page)

24 April 2024

A novel approach to the study of magnetohydrodynamic effect on tritium transport in WCLL breeding blanket of DEMO

Luigi Candido[a*], Ciro Alberghi[a], Fabio Moro[b], Simone Noce[c], Raffaella Testoni[a], Marco Utili[d], Massimo Zucchetti[a,e]

[a]ESSENTIAL Group, Politecnico di Torino – Corso Duca degli Abruzzi, 24, 10129, Torino, Italy
[b]ENEA-FSN, C. R. Frascati – Via E. Fermi 45, 00044, Frascati (RM), Italy
[c] University of Rome Tor Vergata, Industrial Engineering Department – Via del Politecnico, 1, 00133, Rome, Italy
[d]ENEA FSN-PROIN, C.R. Brasimone – Località Brasimone, 40043 Camugnano (BO), Italy
[e]MIT, Massachusetts Institute of Technology, Cambridge (MA), US

The Water-Cooled Lithium Lead (WCLL) breeding blanket is one of the European blanket designs proposed for DEMO reactor. Tritium can permeate into the different structural materials, arising potential issues concerning the fuel self-sufficiency and can be lost into the environment with consequent radiological hazard for the population. Within this frame, a tritium transport analysis is fundamental to evaluate tritium retention in LiPb (15.7 at. % Li) and in the structures and tritium permeation fluxes into the cooling water. To assess this study, a portion of the breeder unit of the outboard equatorial module of the WCLL was modelled. The buoyancy forces and the magnetohydrodynamic (MHD) effect were also included. The final system of partial differential equations was solved with a novel approach through COMSOL Multiphysics. The coupled MHD and heat transfer system of equations was solved performing a transient simulation, that was stopped when the main average variables, temperature and velocity, reached a stable condition. In this way, it was possible to determine the lithium-lead velocity field and to use it as an input for the transport analysis. Tritium transport was modelled by using the input data of tritium generation rate and volumetric power deposition coming from an *ad-hoc* Monte Carlo simulation realized with MCNP software. Moreover, the transport analysis included advection-diffusion of tritium into the LiPb, transfer of tritium from the liquid interface towards the steel, diffusion of tritium inside the steel, transfer of tritium from the steel towards the coolant, advection-diffusion of diatomic tritium into the coolant.

Keywords: DEMO, WCLL, MCNP, MHD, tritium transport

1. Introduction

One of the greatest challenges for the future deployment of fusion electricity is to ensure the tritium self-sufficiency of D-T reactors [1]. The Water-Cooled Lithium-Lead (WCLL) breeding blanket (BB) of the European DEMO reactor is one of its key components which addresses three main functions: neutron shielding, tritium production, heat extraction for electricity production [2]. The WCLL BB adopts pressurized water as coolant and LiPb in eutectic composition (15.7 at. % Li) with the aim of tritium breeder, neutron multiplier and tritium carrier. Within this context, the study of tritium transport inside the blanket is fundamental to correctly assess its design features. Moreover, from the point of view of safety, the amount of tritium permeated towards the coolant and the structural materials to the environment must be kept under a certain level in order to reduce the risk of potential radiological hazard [3].

A considerable amount of literature has been published over the years on tritium transport, both for fusion and fission applications [4]. However, most of these studies focused on a system level approach. So far, very little attention has been paid to the role of a multiphysics approach on the tritium transport phenomenon [5]. In particular, neutronics and magnetohydrodynamics (MHD) need to be studied in order to thoroughly evaluate the LiPb velocity and thermal fields, which strongly affect the tritium transport itself.

In this paper, progresses toward the development of an in-depth 3D predictive model are discussed. A novel computational approach, applied to a portion of the breeder unit of the outboard equatorial module (OB4) of the WCLL, was assessed with COMSOL Multiphysics [6] in order to develop a tritium transport model including the buoyancy forces and the MHD effect. The so-called magneto-convective effect was evaluated under the Boussinesq approximation assuming a toroidal magnetic field intensity equal to 4 T. A dedicated neutronics analysis, performed with MCNP [7], of the tritium generation rate and of the volumetric power deposition was also performed.

The overall structure of this study is hereafter briefly described. Chapter 2 provides an insight of the model and of the computational strategy adopted. Within this frame, the MHD model with buoyancies is deeply explained, along with the neutronics investigation. In Chapter 3, the geometry of the breeder unit and the main input data are presented. Chapter 4 analyses the main outcomes obtained, focusing on tritium concentrations, inventories, permeation rate and tritium partial pressure at the breeder unit outlet. Finally, chapter 5 is dedicated to the summary of this work and the proposals for future research.

2. Numerical methodology

The first step of the numerical approach regards the assessment of the volumetric heat generation rate

(VHGR) or power deposition q_v [W m^{-3}] and the tritium generation rate (TGR) s [mol m^{-3}s^{-1}] performed by means of the MCNP Monte Carlo code complemented with the Joint Evaluated Fusion File JEFF 3.3 nuclear data libraries [8] as main input data. According to [9], a flow chart showing the simplified transport process for a single neutron history is reported in Fig. 1. ROI stands for region of interest, that is the area where the quantities of interest are calculated (in this case, they are the voxels of a mesh used to sample the blanket at equatorial OB level).
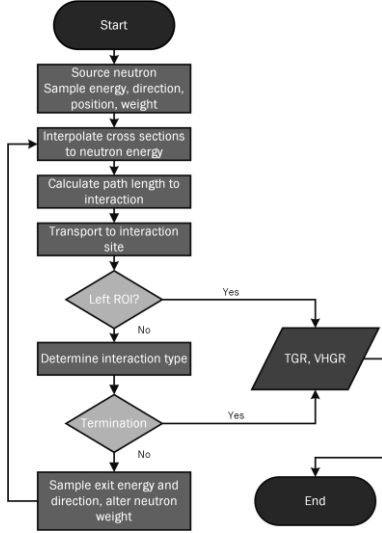

Fig. 1 – Flow diagram for MCNP radiation transport code.

The analyses have been conducted using a semi-heterogenous description of the blanket system based on the segmentation of the breeding blanket into radial sectors with specifically defined material mixture to represent the components embedded in each layer [10]. The resulting functions are both depending on the radial coordinate. The calculation of the power deposition and the TGR is detailed in Chapter 2.3.

The second step of the computational procedure consists of the calculation of the mixed MHD/heat transfer (magneto-convection) profiles. The MHD/heat transfer study solves the temperature, potential and current fields only in the LiPb and in the baffle, in order to represent the electrical coupling between the upper and lower parts of the submodule. The other domains are included considering appropriates boundary conditions, as detailed afterwards. The time-dependent magneto-convective flows involves the Navier-Stokes equation of mass continuity and momentum conservation under Boussinesq's hypothesis, the Ohm's law, the electric current conservation and the heat transfer equation. These lead to the following system of partial differential equations:

$$\nabla \cdot \boldsymbol{u} = 0 \tag{1}$$

$$\rho \frac{\partial \boldsymbol{u}}{\partial t} + \rho(\boldsymbol{u} \cdot \nabla \boldsymbol{u})$$
$$= -\nabla p + \mu \nabla^2 \boldsymbol{u} + \boldsymbol{J} \times \boldsymbol{B} + \rho \boldsymbol{g}[1 - \beta(T - T_0)] \tag{2}$$

$$\nabla \cdot \boldsymbol{J} = 0 \tag{3}$$

$$\boldsymbol{J} = \sigma(-\nabla\Phi) + \sigma(\boldsymbol{u} \times \boldsymbol{B}) \tag{4}$$

$$\rho c_p \frac{\partial T}{\partial t} + \rho c_p (\boldsymbol{u} \cdot \nabla)T = k\nabla^2 T + q_v \tag{5}$$

where ρ [kg m^{-3}] is the density, $\boldsymbol{u}$ [m s^{-1}] is the velocity vector, p is the pressure field [Pa], μ [Pa s] is the dynamic viscosity, $\boldsymbol{J}$ [A·m^{-2}] is the current density, $\boldsymbol{B}$ [T] is the magnetic flux density, $\boldsymbol{g}$ [m·s^{-2}] is the gravity vector, β [K^{-1}] is the volumetric thermal expansion coefficient, σ [S·m^{-1}] is the electric conductivity of the lithium-lead, ϕ [V] is the electric potential, T [K] is the temperature, c_p [J kg^{-1} K^{-1}] is the specific heat at constant pressure, k [W m^{-1} K^{-1}] is the thermal conductivity and q_v [W m^{-3}] is the volumetric heat generation rate or volumetric power deposition.

The transient simulation of the magneto-convection was stopped when the average temperature dropping rate of the LiPb domain was such that $\partial \bar{T}_{LiPb}/\partial t < 0.01$ [K s^{-1}]. This means that the ratio between the internal energy loss Q_{loss} [W] and the total volumetric heating power Q_{tot} [W] is less than 1%, i.e.:

$$\frac{Q_{loss}}{Q_{tot}} = \iiint_{\Omega_{LiPb}} \rho c_p \frac{\partial T}{\partial t} dV \Big/ \iiint_{\Omega_{LiPb}} q_v \, dV \tag{6}$$

An educated guess on the initial value of the average temperature ($T_{guess} = 650$ [K]) helped to reduce the transient time needed to stabilize the temperature fluctuations. For all the meshes considered, this transient time is between 80 and 90 seconds. Moreover, the average velocity fluctuations around the mean value reached a maximum deviation of ± 0.1 [mm s^{-1}]. Once the variables were stabilized, to ensure a minimum discretization error, a grid convergence study was carried out according to the procedure exposed by Roache et al. [11] and Celik et al. [12] and suggested within the ERCOFTAC Best Practice Guidelines for Industrial Applications [13]. The criterion to choose the best mesh was set for the average GCI index to be lower than 5%. A flow diagram of the MHD/heat transfer solution is given in Fig. 2.
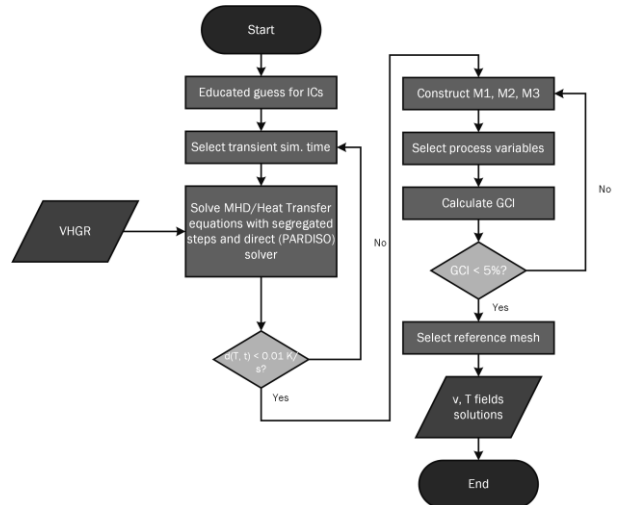

*Fig. 2 – Flow diagram for MHD/heat transfer solution.*

The last step consists of the solution of the general tritium transport equation and the evaluation of the tritium

concentration in the lithium-lead, in the Eurofer pipes and structures and in the water pipes, along with the permeation flux into the coolant. As far as tritium concentration and permeation flux into the coolant are concerned, it was needed to solve the turbulent flow in the water domain, in order to assume the correct water velocity profile. For this reason, a $k - \omega$ turbulent model was chosen, and an iterative procedure was adopted until the wall resolution was below 100 viscous units. Finally, a passive, scalar, general tritium transport equation (GTE) could be written as follows:

$$\frac{\partial c}{\partial t} + (\nabla \cdot \vec{u})c + \nabla \cdot (-D\nabla c) = s \qquad (7)$$

where c [mol·m^{-3}] is the tritium concentration in the i-th domain (lead-lithium, Eurofer, water), D [m^2·s^{-1}] is the diffusion coefficient of tritium and s [mol·m^{-3}·s^{-1}] is the molar tritium generation rate along the radial coordinate. The velocity profile of lithium-lead and water, as well as the temperature fields for the properties evaluation, were

obtained from the previous steps and used as an input to the GTE. Once monoatomic tritium recombines in diatomic form, it interacts with the naturally solved hydrogen present in water according to the chemical reactions:

$$H_2 + T_2 \rightleftarrows 2HT \qquad (8)$$

$$HT + H_2O \rightleftarrows H_2 + HTO \qquad (9)$$
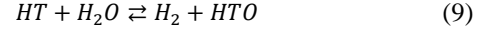
Following the approach proposed in [14], an *a posteriori* chemical analysis was implemented in this study. It was assumed as a simplifying approach that chemical equilibrium occurs; for both Equation (8) and (9), the chemical equilibria constants have been derived from [15] and [16], respectively. The profile of the recombined tritium was then used as an input for the chemical calculation. For the sake of clarity, a block diagram regarding the solution algorithm procedure is shown in Fig. 3.
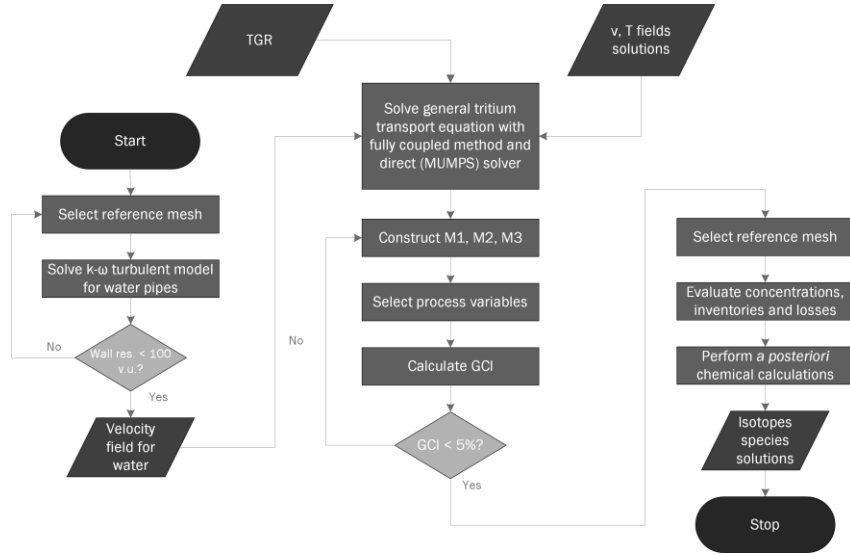

Fig. 3 – Flow diagram for tritium transport calculation.

2.1 Grid convergence analysis

The Grid Convergence Index method (GCI) is a recommended method evaluated over several hundred computational cases. Three different hybrid meshes were used, labeled M1 (finest), M2 (reference mesh) and M3 (coarser). A grid refinement factor, i.e. the ratio between the characteristic mesh element size between the finer to the coarser mesh higher than 1.3 was adopted:

$$r = \frac{h_{coarser}}{h_{finer}} = \frac{\left(\frac{1}{N_{coarser}}\sum_i \Delta V_{i,coarser}\right)^{1/3}}{\left(\frac{1}{N_{finer}}\sum_i \Delta V_{i,finer}\right)^{1/3}} \qquad (10)$$

Here, h [mm] is the characteristic mesh size, N is the total number of elements and ΔV [mm^3] is the mesh volume. This means, that the number of elements of the fine mesh has about twice the number of elements of the reference mesh, as well as for the reference mesh with respect to the coarse mesh. The meshes were uniformly coarsened in the three directions as suggested in the grid independence procedure. In this way, the elements number has a monotonically decreasing trend, as detailed

in Fig. 4 and Fig. 6. The reference quality for the mesh is the condition number [17], which is based on mathematical properties of the matrix transforming the actual element to an ideal element. More details on quality measurement associated to the condition number can be found in [18].

As far as the magneto-convection analysis is concerned, the thickness of the first layer of the Hartmann walls δ_{Ha} [mm] and of the side walls δ_{side} [mm] were halved from the coarser mesh to the finer mesh ($\delta_{Ha} = 0.01, 0.02, 0.04$ mm and $\delta_{side} = 0.1, 0.2, 0.4$ mm for M1, M2, M3, respectively). The thickness of the succeeding layers was increased by 25%. The mesh details are reported in Fig. 4. The total number of elements for M1 is 273926.
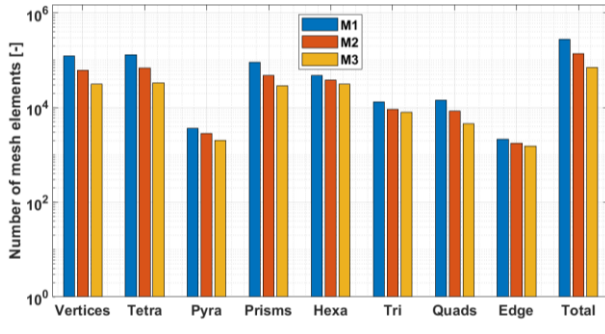
Fig. 4 – Mesh statistics for the magneto-convection study.

A total of 10 variables, both local and global, were selected and reported in Table 1; the calculated Grid Convergence Indexes (GCIs) are graphically reported in Fig. 5, where the comparison between M1 with respect to M2 and between M2 to M3 is shown. For the best mesh, M1, the maximum Grid Convergence Index is 4.95% and is found for the LiPb velocity averaged on the LiPb domain (ID6); the average GCI is 1.15%, instead of 4.08% of the case M2/M3. Hence, M1, characterized by a condition number of 0.766, is used as the reference mesh for the MHD/heat transfer studies.

Table 1 – Variable selection for magneto-convection analysis.

| ID	Variable	Type
1	Max. LiPb velocity on volume	Local
2	Max. LiPb velocity on surface	Local
3	Max. LiPb temperature	Local
4	Max. Eu temperature	Local
5	Max. current density	Local
6	Average LiPb velocity on volume	Global
7	Average LiPb velocity on surface	Global
8	Average LiPb temperature	Global
9	Average Eurofer temperature	Global
10	Average pressure on volume	Global
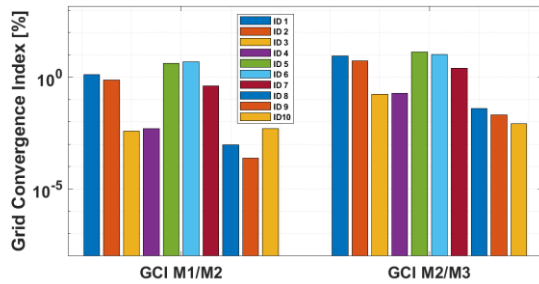
Fig. 5 – Grid Convergence Index for the magneto-convection study.

In a similar way, the grid convergence analysis for the transport simulation was conducted. The mesh statistics are displayed in Fig. 6. The total number of elements for the best mesh is 864049, with a quality of 0.774.
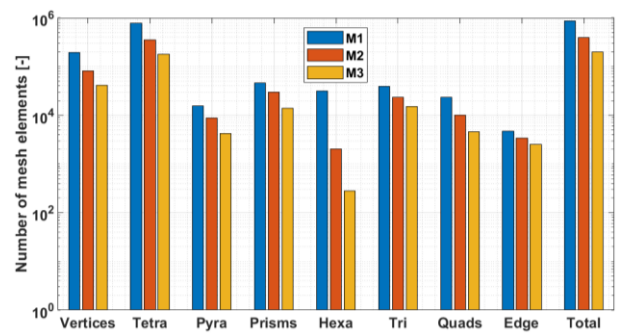

Fig. 6 – Mesh statistics for the transport study.

For the transport analysis, a total number of 9 variables was chosen according to Table 2. The GCI calculation, shown in Fig. 7, presents a maximum GCI of 9.99% for the average LiPb velocity on volume and an average GCI for the mesh M1 with respect to M2 equal to 3.24%. Even for the transport studies, the mesh M1 was chosen as the reference (the GCI of M2 with respect to M3 is 3.95%). It should be noticed that only 3 out of 9 variables (ID 4, 8, 9) showed a lower GCI index of M1/M2 with respect to M2/M3. This is a sign of oscillatory convergence intrinsically connected to the apparent order of the method. However, it should be kept in mind that the GCI analysis has the capability to treat oscillatory convergences, as detailed in [13], which can easily occur in CFD studies. The error estimate takes into account such oscillations; for this reason, maximum errors below 10% and average ones below 5% can be considered acceptable for the purpose of this work.

Table 2 – Variables selection for transport analysis.

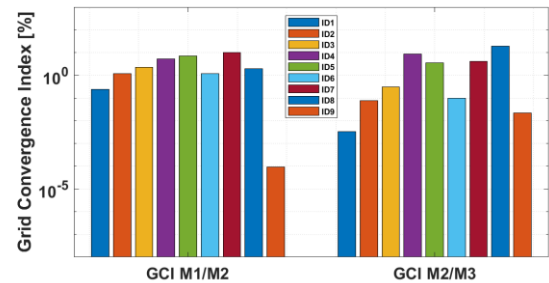| ID	Variable	Type
1	Max LiPb conc. on volume	Local
2	Max Eu conc. on volume	Local
3	Max Water conc. on volume	Local
4	Average LiPb conc. on volume	Global
5	Average Eu conc. on volume	Global
6	Average Water conc. on volume	Global
7	Average LiPb velocity on volume	Global
8	T permeation rate to Eu	Global
9	T permeation rate to Water	Global

Fig. 7 – Grid Convergence Index for the transport study.

2.2 Monte Carlo calculation

The present WCLL BB layout [2] relies on a Single-Module-Segment (SMS) concept where the breeding unit (BU), is replicated in inboard and outboard along the

poloidal direction. Each BU (Fig. 8) includes the first wall (FW) and side walls, top and bottom caps, internal stiffening and baffle plates, BSS, cooling pipes, LiPb manifolds and water manifolds for FW and breeding zone cooling.
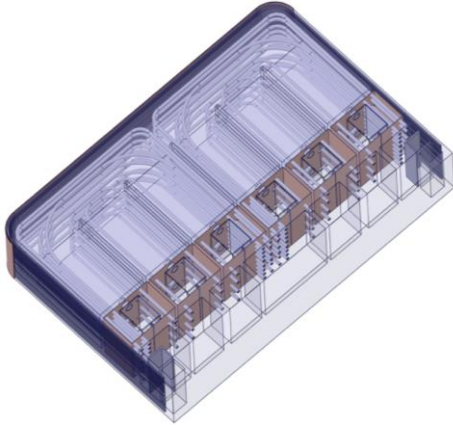

Fig. 8 – WCLL BU: perspective view of the outboard breeding unit, showing the inner cooling pipes layout.

Taking into account the complex layout of the BU cooling pipes assembly, the modeling approach to generate an equivalent geometry suitable for the MCNP calculations is based on the segmentation of the BB structure into radial sectors with different material mixture. The obtained MCNP WCLL BB layered model has been successively integrated into the EU DEMO1 2017 reference configuration model (Fig. 9), representing a 11.25° toroidal sector of the tokamak [19], with plasma parameters shown in Table 3.
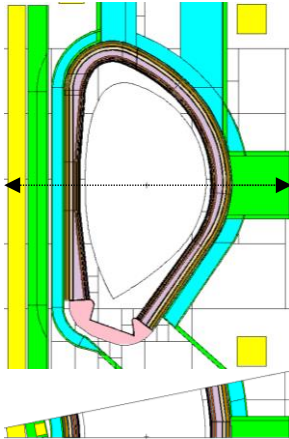

Fig. 9 – WCLL DEMO MCNP model: poloidal section showing the inboard and outboard breeding blanket (top picture) and toroidal section along the equatorial plane (bottom picture).

Table 3 – Main parameters of the EU DEMO1 2017 baseline.

Parameter	Value
N° of Toroidal Field Coils	16
Major radius (m)	8.938
Minor radius (m)	2.883
Aspect ratio	3.1
Plasma elongation	1.65
Plasma triangularity	0.33
Fusion power	1998
Average neutron wall loading (MW m^{-2})	1.04
Net electric power (MW)	500

The MCNP DEMO model integrating the WCLL blanket so far described has been used to assess the TGR and the nuclear heating density radial profiles on the equatorial mid plane, corresponding to the OB4 module in the previous WCLL BB layout based on a Multi-Module-Segment configuration [20]. The simulations have been performed using standard MCNP cell-based (F4, F6 tallies) and mesh tallies (FMESH tally) with proper multipliers to calculate the specific nuclear responses; results are normalized to 1998 MW fusion power (neutron yield: $7.095 \cdot 10^{20}$ n s^{-1}), according to the plasma parameters specified in Table 3.

The outcomes of the performed analyses are shown in Fig. 10 and Fig. 11, where the radial profiles of the TGR and nuclear heating density are reported respectively. As far as the TGR is concerned, most of the Tritium is generated in the area of the BU closer to the FW (first 20 cm), while the behavior tends to flatten in the back region of the breeding zone up to the LiPb manifolds.
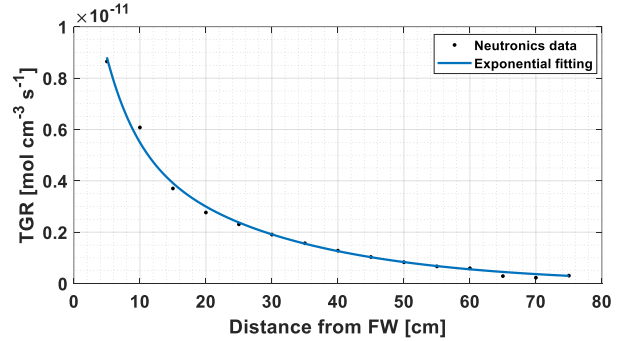

Fig. 10 – Radial profile of the TGR calculated in outboard up to the LiPb manifolds.

The neutronics data can be fitted by the double-exponential function:

$$s = 1.044 \cdot 10^{-11} \cdot e^{(-0.2182 \cdot x_{FW})} + \\ 6.514 \cdot 10^{-12} \cdot e^{(-0.04106 \cdot x_{FW})} \quad (11)$$

where s [mol cm^{-3}s^{-1}] is the TGR in radial direction and x_{FW} [cm] is the distance from the first wall. The R-square value is 0.9956.

The power deposition radial profile presents a maximum value of 28.4 W/cm^3 at the FW Tungsten armour, decreasing up to 0.4 W/cm^3 and 0.06 W/cm^3 on LiPb and Eurofer respectively, in the area of BU closer to the manifolds. The volumetric power deposition, expressed as [W cm^{-3}], in the LiPb can be represented as:

$$q_v = 25.53 \cdot e^{(-0.5089 \cdot x_{FW})} + 5.443 \cdot e^{(-0.0879 \cdot x_{FW})} \quad (12)$$
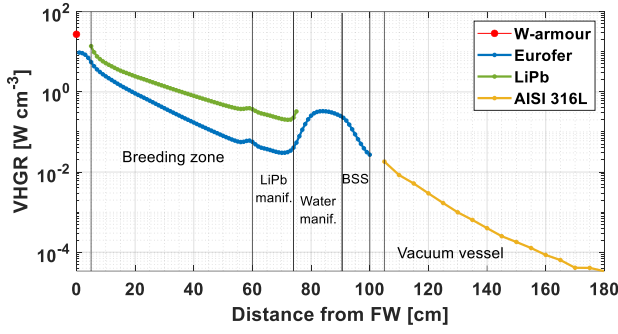
with an R-square value of 0.9998.

Fig. 11 – Breakdown of the nuclear heating density radial profile calculated for the W armour, Eurofer, LiPb and AISI 316L at the outboard equatorial plane.

3. Geometry and input data

As highlighted in the previous paragraph, the SMS approach permits to have a single breeding element (breeder unit, BU) repeated along the poloidal direction. The breeder unit is symmetric with respect to the radial-poloidal plane and the radial-toroidal plane, such that the reference geometry can be assessed as 1/4 of the BU [21]. Within this work, one sixth of the reference geometry is simulated due to the in-house computation resources availability. The central submodule was analysed as shown in Fig. 12. A radial-poloidal section is represented in Fig. 13, where the LiPb flow path is shown.
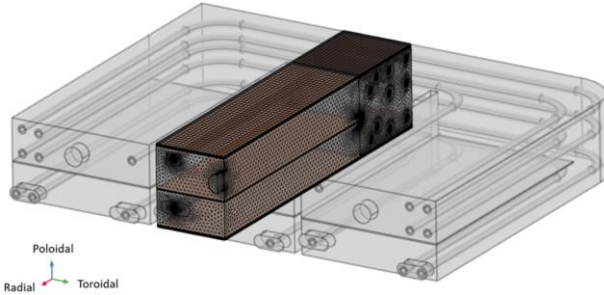

Fig. 12 – Representation of a WCLL breeder unit reference geometry (in gray) and the simulation domain (in dark) relative to the central outboard equatorial module.
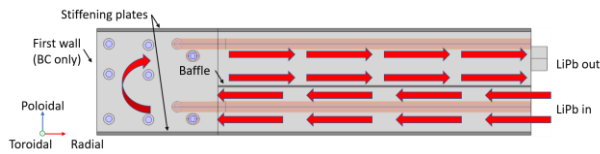

Fig. 13 – Radial-poloidal section of the analyzed geometry.

Concerning the MHD/heat transfer computation, the heat transfer between the water flowing in the toroidal and radial-toroidal pipes and the lithium-lead was modelled with an effective thermal conductance or global Heat Transfer Coefficient, HTC [W m^{-2}K^{-1}]:

$$HTC = \left(\frac{1}{h_{Eurofer}} + \frac{1}{h_{water}} \right)^{-1} \qquad (13)$$

where $h_{Eurofer} = 2k_{Eurofer}/d_{int} \ln(d_{ext}/d_{int})$ and h_{water} was evaluated with Dittus-Boelter correlation [22] for turbulent flow in smooth pipes. Eq. (13) provides an

effective thermal conductance equal to 5514 W m^{-2}K^{-1} evaluated at the inlet water velocity. A calculation at the average water pipe velocity would have provided a value which departs of less than 4% from the present value. The main geometrical parameters are reported in Table 4.

Table 4 – Main geometrical parameters for WCLL reference geometry of BU used in the computation.

Parameter	Description	Value [mm]
L_r	Radial length	540
L_p	Poloidal length	132
L_{tor}	Toroidal length	116.5
d_{ext}	Pipes external diameter	13.5
d_{int}	Pipes internal diameter	8
D_{LiPb}	Outlet LiPb diameter	30
t_{baffle}	Baffle thickness	2
t_{SP}	Stiffening plates thickness	4
H_d	Height of PbLi channel, inlet	55.5

An overview of the main thermophysical properties for LiPb [23] and Eurofer97 [24] are reported in Table 5. As far as transport properties are concerned [25]–[28], Table 6, it should be noticed that recombination and dissociation constants of Optifer-IVb were assumed, according to [29] and [30]. In COMSOL, the temperature-dependent correlations were implemented.

Table 5 – Thermophysical properties of LiPb and Eurofer97 evaluated at $T = 700$ K.

Parameter	LiPb	Eu97	Units
Density, ρ	9687	7623	[kg m^{-3}]
Specific heat, c_p	188.6	600.7	[J kg^{-1}K^{-1}]
Th. Conductivity, k	22.89	29.40	[W m^{-1}K^{-1}]
Dyn. viscosity, μ	1.555	-	[mPa s]
El. conductivity, ρ_{el}	$8.397 \cdot 10^5$	$1.015 \cdot 10^6$	[S m^{-1}]

Table 6 – Transport properties of LiPb and Eurofer97 evaluated at $T = 700$ K.

Parameter	Value	Units
LiPb		
Sieverts' constant, Reiter $k_{S,R}$	$1.024 \cdot 10^{-3}$	[mol m^{-3}Pa$^{0.5}$]
Sieverts' constant, Aiello $k_{S,A}$	$2.608 \cdot 10^{-2}$	[mol m^{-3}Pa$^{0.5}$]
Tritium diffusivity, D_{LiPb}	$1.413 \cdot 10^{-9}$	[m^{2}s^{-1}]
Eurofer97		
Sieverts' constant, $k_{S,Eu}$	$1.680 \cdot 10^{-3}$	[mol m^{-3}Pa$^{0.5}$]
Recombination constant, $k_{r,Eu}$	$2.055 \cdot 10^{-9}$	[m^{4}mol^{-1}s^{-1}]
Dissociation constant, $k_{d,Eu}$	$1.975 \cdot 10^{-10}$	[mol s^{-1}m^{-2}Pa^{-1}]
Tritium diffusivity, D_{Eu}	$5.721 \cdot 10^{-9}$	[m^{2}s^{-1}]

The main dimensionless parameters characterizing the MHD buoyant flow are summarized in Table 7. The

magnetic Reynolds number is defined as $Rm = u_0 L/\eta = \tau_\eta/(L/u_0) = \tau_\eta/\tau_d$ where τ_η is the electromagnetic diffusion time scale and τ_d is called dynamic time scale. When Rm is large ($Rm \gg 1$), diffusion is weak, and the magnetic field lines are like elastic bands frozen into the conducting medium. On the other hand, if $Rm \ll 1$ the magnetic field is mainly diffused, and it remains unaffected by $\boldsymbol{u}$. The system of Eqs. (1)-(5) are then justified since $Rm \sim O(10^{-5})$. The LiPb eutectic liquid metal is characterized by a low value of the Prandtl number, which is typical of free-flowing liquid metals with high thermal conductivity. According to [31], the characteristic MHD velocity, u_0, was chosen such that the Lorentz forces balance the buoyancy forces. To do so, a characteristic temperature difference ΔT was introduced:

$$\Delta T = \frac{L^2}{k} \cdot \frac{1}{V} \iiint_{\Omega_{LiPb}} q_v \, \mathrm{d}V \qquad (14)$$

where L [m] is the characteristic length of the BU chosen as half of the toroidal length, according to the direction of the external magnetic field. The magnetic field is assumed to be uniform in space and constant in time, such that $\boldsymbol{B} = B_0 \boldsymbol{L_{tor}}/L_{tor}$, with $B_0 = 4$ T. The characteristic MHD velocity is proportional to the characteristic temperature difference: introducing the Grashof number, it is possible to demonstrate that:

$$u_0 = \frac{Gr}{Ha^2} \frac{\nu}{L} \qquad (15)$$

where $\nu = \mu/\rho$ [m^{2}s^{-1}] is the kinematic viscosity and Ha is the Hartmann number. For the present case, $Ha = 10830$, hence Lorentz forces are dominant with respect to the viscous ones, which are confined in the Hartmann layers (perpendicular to the magnetic field) and side layers (parallel to the magnetic field) of thickness $\delta_{Ha} \sim O(Ha^{-1})$ and $\delta_{side} \sim O(Ha^{-1/2})$, respectively. The characteristic velocity is reduced up to 0.5614 [mm s^{-1}]. The damping effect on the flow features is evident when considering the Reynolds number. For the pure hydrodynamic case, the characteristic velocity can be estimated as $u_{hyd} = \sqrt{Gr} \, \nu L = 301.2$ [mm s^{-1}]; hence, the flow would be turbulent, being characterized by $Re_{hyd} \sim O(10^5)$. On the contrary, for the MHD case the LiPb flow is laminar with $Re \sim O(10^2)$, and dominated by natural convection ($Ri \sim O(10^5)$).

The ratio between the electromagnetic force and the buoyancy force is expressed by Lykoudis number, which represents the fact that the buoyancy force is damped as Ha increases [32]. From a physical viewpoint, $Ly \gg 1$ means that the velocity oscillations induced by the strong temperature gradients are hindered by the action of the external magnetic field. The square of the Lykoudis number is the interaction parameter N, which for this case is $O(10^5)$, highlighting that the inertia forces are much smaller when compared to Lorentz forces.

Finally, another dimensionless number adopted is the Péclet number, which expresses the ratio of the advective transport rate to the diffusive transport rate. It is possible to demonstrate that the inertial terms in Eq. (2) and Eq. (4) can be neglected when $Ly \gg 1$ and $Pe \ll 1$, respectively. For this case, $Pe \gg 1$, hence the inertia terms are maintained in the heat transfer equation. However, as stated in [33], the inertia effects cannot be neglected in the momentum balance if high velocity jets are expected at side boundary layers. Taking into account this recommendation, the full system of Eqs. (1)-(5) is solved.

Table 7 – Dimensionless numbers characterizing the magneto-convective flow.

Name	Symbol	Definition	Significance	Value
Reynolds number	Re	$u_0 L/\nu$	Inertia/viscous forces	407.4
Interaction parameter	N	$\sigma_m B_0^2 L/\rho u_0 = Ly^2$	Lorentz forces/inertia	$2.878 \cdot 10^5$
Hartmann number	Ha	$B_0 L(\sigma_m/\rho\nu)^{1/2} = (NRe)^{1/2}$	(Lorentz forces/viscous forces)$^{1/2}$	10830
Magnetic Reynolds number	Rm	$u_0 L/\eta$	Advection/diffusion of $\boldsymbol{B}$	$6.902 \cdot 10^{-5}$
Grashof number	Gr	$g\beta\Delta T_0 L^3/\nu^2 = Re \cdot Ha^2$	Buoyant forces/viscous forces	$4.778 \cdot 10^{10}$
Lykoudis number	Ly	$Ha^2 Gr^{-0.5}$	Lorenz forces/buoyant forces	536.5
Prandtl number	Pr	ν/α	Momentum diff./thermal diff.	$1.281 \cdot 10^{-2}$
Rayleigh number	Ra	$Gr \cdot Pr$	Diff. transport rate/Conv. transport rate	$6.122 \cdot 10^8$
Richardson number	Ri	Gr/Re^2	Natural convection/forced convection	$2.878 \cdot 10^5$
Péclet number	Pe	$Re \cdot Pr = Gr \cdot Pr/Ha^2$	Adv. transport rate/diff. transport rate	5.221
Wall conductance ratio	c_w	$\sigma_w t_w/\sigma L$	Walls conductance/LiPb conductance	0.2940

The main boundary conditions, in addition to those already reported in the previous paragraph, are reported in Table 8. The details of the BCs adopted for the tritium transport analysis, as well as those adopted for the chemical computation, are thoroughly detailed in [14] and [34].

Table 8 – Main input data.

Parameter	Description	Value
$T_{in,LM}$	Lead-lithium inlet temp.	325 [°C]
p_{LM}	Lead-lithium inlet pressure	5 [bar]
v_{LM}	Lead-lithium inlet velocity	0.178 [mm $\cdot$ s^{-1}]
Φ_{FW}	Thermal heat flux at FW	-130 [kW $\cdot$ m^{-2}]
$T_{in,w}$	Water inlet temperature	285 [°C]
$v_{w,BZ}$	Water inlet velocity in BZ	1.30 [m $\cdot$ s^{-1}]
p_w	Water inlet pressure	155 [bar]

4. Results and discussion

The aim of the previous sections was to illustrate the novel computational approach for the resolution of the general tritium transport equation, taking into account the temperature and velocity fields which result from the MHD effect. To do so, the integration of the neutronics analysis was necessary, with the aim of deriving the main inputs necessary for both the heat transfer equation and the GTE.

4.1 MHD/heat transfer

Fig. 14 presents the velocity field on the middle radial-poloidal plane of the center sub-module. To better visualize the results, a zoom in the region between the first wall and the baffle is shown, with a filter up to 20 mm s^{-1} in order to highlight the velocity patterns. In this way, higher velocities are represented in red. The flow presents several recirculation zones due to the buoyancy-driven MHD flow in proximity of the water pipes, characterized by LiPb velocities up to 10 mm s^{-1}. Velocity jets arise near the FW and near the stiffening plates, with spikes up to 55 mm s^{-1}. The backflow at the outlet experienced in [21] was suppressed by adding to the computational domain the outlet LiPb pipe, as displayed in Fig. 15. To solve the Ha layer, no wall functions were considered. The velocity field was solved up to the wall.
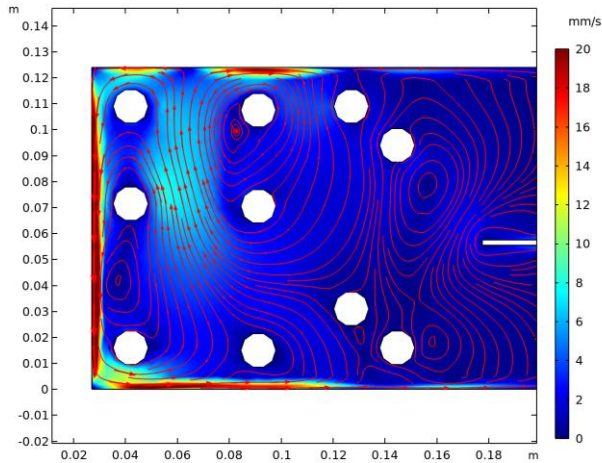

Fig. 14 – View of the zone between FW and baffle on a radial-poloidal cut at the middle of the central submodule.
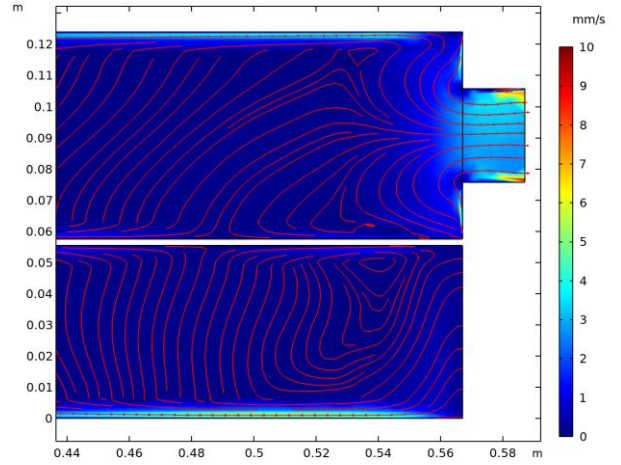

Fig. 15 – View of the zone LiPb inlet/outlet on a radial-poloidal cut at the middle of the central submodule.

In Fig. 16, the temperature field is shown. The temperature distribution presents a temperature gradient of 98 °C in the zone between the FW and the baffle, whereas it is more uniform in the rest of the BU, with the exception of the entry region. The maximum temperature in the LiPb is 394 °C and is localized in the central part of the module where only two pipes provides the cooling action. This value is lower with respect to [5] or [32] due to several reason. Firstly, only a small part of the BU is analysed, for which the thermal behaviour of the adjacent submodules is not taken into account. Secondly, the volumetric power deposition is much lower with respect to [21] (up to 3 times in the maximum value of the VHGR) and in accordance with [5]. Finally, the FW boundary condition was changed according to [5] and [32]. The maximum temperature reached in the central submodule of the BU is below the Eurofer97 temperature limit of 550 °C and below the corrosion temperature limit of 475 °C.
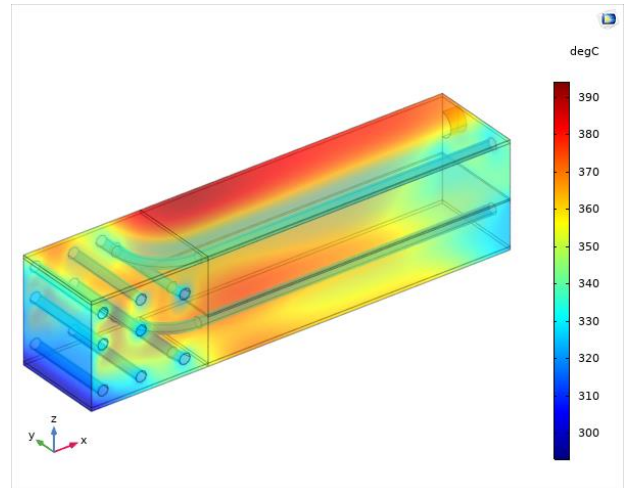

Fig. 16 – 3D temperature distribution in the simulated geometry of the WCLL breeder unit.

The electric potential for the poloidal-toroidal plane located at the LiPb inlet/outlet is shown in Fig. 17. The picture is mirrored with respect to the radial-poloidal plane to highlight the symmetry. Compared to [5], the piping was not directly simulated, instead a thin-wall

boundary condition was adopted. In addition, the reference geometry adopted for this study has less pipes and different BCs for the stiffening plates. It should be pointed out that the latter BC does not consider the electrical coupling between near submodules. This, as shown by different authors (see for instance Mistrangelo and Buhler [35], [36]), has an impact on the flow characteristics – and consequently on tritium transport – and will be considered in further analysis. The electrical coupling between the upper and lower parts of the submodule was considered
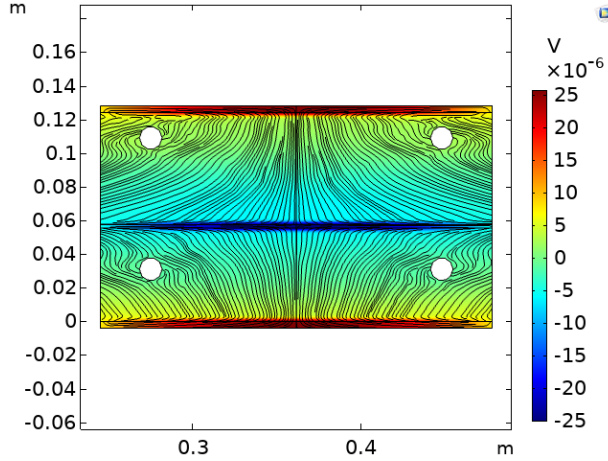

Fig. 17 – Electric potential with current density streamlines on the poloidal-toroidal plane locate at LiPb inlet/outlet.

A summary of the main MHD/heat transfer results is reported in Table 9.

Table 9 – Main magneto-convection results.

	Maximum	Average
LiPb temperature [°C]	394	360
LiPb velocity [mm s^{-1}]	55.0	1.05
Water velocity [m s^{-1}]	1.69	1.18
Temperature at LiPb outlet [°C]	367	363
Velocity at LiPb outlet [mm s^{-1}]	9.60	3.36

4.2 Tritium transport

Tritium transport calculations have been carried out assuming DEMO to be operated at steady-state conditions. Moreover, Reiter's [25] and Aiello's [26] correlations for Sieverts' constant were assumed. Fig. 18 shows the concentration distribution after 7 days (total computational time for Reiter's case) plotted over the total flux streamlines. Most of tritium is generated in the zone between the first wall and the baffle, with a maximum value of $0.340 \, \text{mol m}^{-3}$; this leads to the highest concentrations of the whole BU. The tritium concentration increases with time and decreases exponentially with the radial coordinate. The concentration distribution is strongly influenced by the velocity distribution as can be seen in Fig. 14 and is increased due to the presence of recirculation zones which increments the tritium mean permanence time.
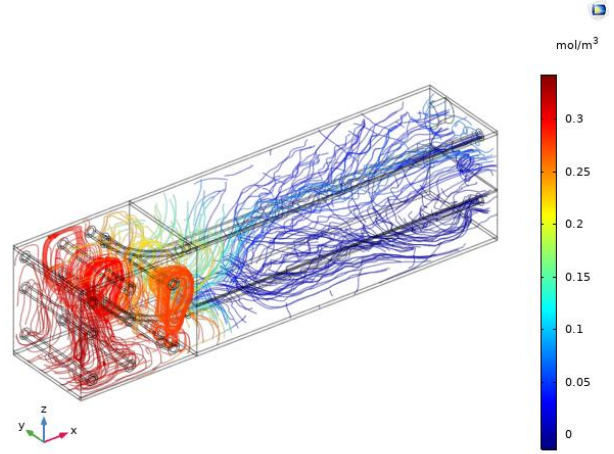

Fig. 18 – 3D concentration distribution in the simulated geometry of the WCLL breeder unit, Reiter correlation.

Most of tritium permeating into the cooling water tends to form tritiated water, HTO, due to the addition of hydrogen (8 wppm) for the water chemistry. Traces of HT and T_2 are present. As far as the HTO concentration is concerned, in Fig. 19 a sketch representing the nomenclature of the different pipes is reported, whereas in Fig. 20 the HTO concentration evolution for each pipe is shown. The highest concentration is found in pipes (3,1) and (3,2), i.e. in the bottom part of the simulated geometry near the FW, where velocity spikes are higher. The concentrations values are 0.565 and 0.557 mol m^{-3}, respectively. The pipes with lower concentrations are pipes A and B, which present a radial-poloidal path, with concentrations of 0.145 and 0.197 mol m^{-3}, respectively. This is due to the fact that the tritium generation rate is much lower in the region of the baffle and near the LiPb inlet/outlet with respect to the zone between the FW and the baffle. The HTO concentration averaged on all the water pipes is 0.332 mol m^3.
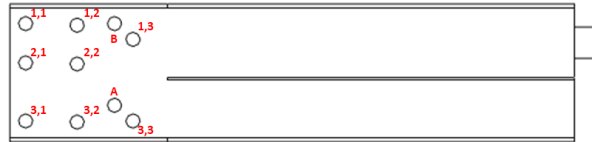

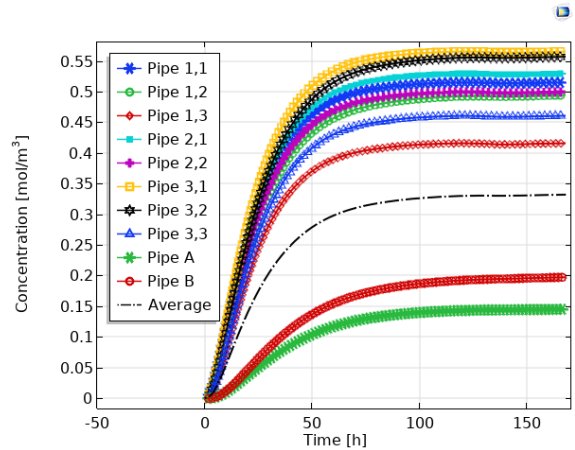
Fig. 19 – Pipes nomenclature.

Fig. 20 – HTO concentration in water pipes, Reiter correlation.

In Fig. 21 the evaluations of tritium inventories are reported according to Reiter's and Aiello's correlations for Sieverts' constant. The assumption of Aiello's correlation is more conservative, leading to a total inventory of 9.37 mg of tritium against 2.72 mg as calculated with Reiter's correlation. According to Aiello's constant results most of tritium is found in the Eurofer components (pipes, stiffening plates and baffle). Reiter's correlation tends to underestimate the inventories in Eurofer domains and in water up to one order of magnitude. Moreover, Reiter's correlation ensures faster response time. For instance, the 99% equilibrium time to reach the asymptotic inventory value for LiPb is 39 h in case of Reiter's, whereas 289 h for Aiello's.
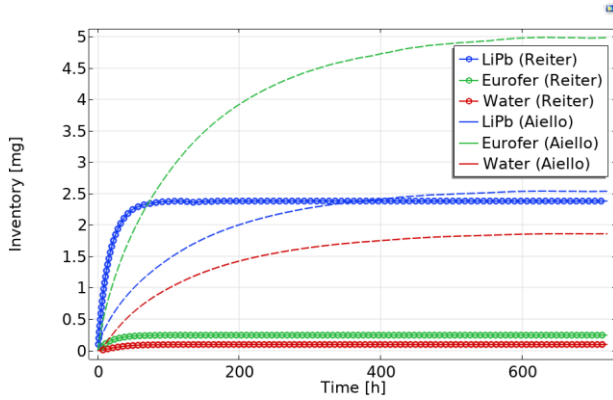

Fig. 21 – Tritium inventories for Reiter and Aiello correlations.

Tritium permeation rates to water pipes are reported in Fig. 22 according to both the correlations adopted for the evaluation of the Sieverts' constant. The trend of the permeation rates initially increases up to a maximum, then it decreases up to an asymptotic value. In this case, the dissociation flux, at a certain point, tends to become dominant with respect to the recombination flux as long as a new equilibrium is reached. This can be confirmed by the low value of the permeation parameter [37], which, according to the transport proprieties taken from [27] and [28], is $\sim O(10^{-4})$, hence characteristic of a surface-limited regime. Further investigations on this point will be carried out as a future work.
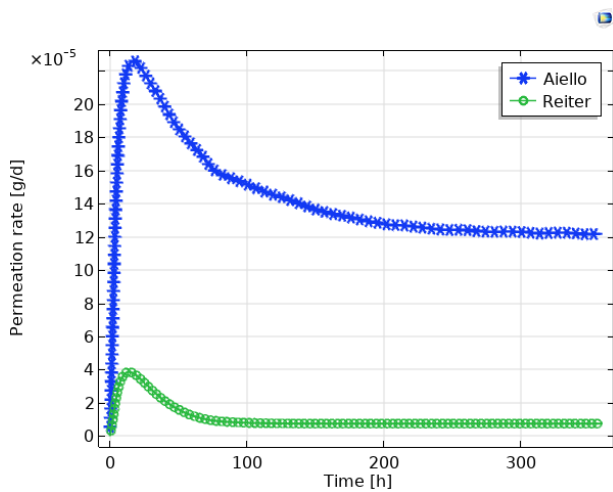

Fig. 22 – Tritium permeation rates.

Tritium partial pressure inside the LiPb can be evaluated according to Sieverts' law as:

$$p = \left(\frac{c}{k_S}\right)^2 \qquad (16)$$

where c [mol m^3] is the concentration of tritium inside the LiPb and k_S [mol m^{-3} Pa$^{-0.5}$] is the Sieverts' constant of tritium solubilized in the liquid metal. The results of the calculation are reported in Fig. 23. It can be seen that according to the Sieverts' constant correlation adopted, the spread between the resulting tritium partial pressure can achieve a difference of more than 2 orders of magnitude. The value for the equilibrium pressure adopting Reiter's correlation is 617 Pa, whereas for Aiello's is 2.80 Pa. A resume of the main tritium transport results is reported in Table 10.

Table 10 – Main transport results.

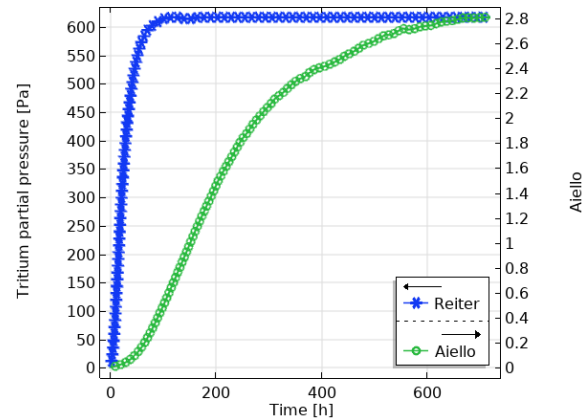| Reiter	c [mol m^{-3}]	I [mg]	t_{eq}^* [h]
T in LiPb alloy	0.106	2.38	39
T in Eurofer	0.106	0.245	42
HTO in water	0.332	0.0960	61
Aiello			
T in LiPb alloy	0.113	2.53	289
T in Eurofer	2.16	4.98	308
HTO in water	6.43	1.86	324

Fig. 23 – Tritium partial pressure at LiPb outlet.

5. Conclusions and future work

In this work, a novel approach to the study of the MHD on the transport of tritium for a WCLL breeder unit was presented. The multiphysics nature of the transport phenomenon required to develop a numerical methodology able to incorporate the results from the neutronics and from the magnetohydrodynamics. This kind of approach permitted to have a tool able to calculate the tritium retention in the different materials, the permeation fluxes to the water and the partial pressures taking into account the different physics involved.

In particular, from the neutronics analysis the radial distribution of the tritium generation rate and of the volumetric power deposition was calculated. The VHGR was used as an input for the magneto-convective analysis, whereas the TGR was the input for tritium transport study.

The MHD analysis highlighted that spike velocities up to 55 mm s^{-1} are present near the first wall and in proximity of the stiffening plates, where the volumetric heat generation rate assumes higher values and the temperature gradients are greater. This determines the creation of recirculation patterns characterized by velocities up to 10 mm s^{-1}. The backflow experienced in other works [21] was suppressed. Concerning the temperature field, a temperature gradient of 98 ℃ exists in the zone between the first wall and the baffle, while it is almost uniform in the rest of breeder unit, with a maximum temperature of 394 ℃, well below the temperature limit for Eurofer both from the mechanical point of view and from the corrosion point of view.

The transport study was performed adopting Reiter's and Aiello's correlations for the calculation of Sieverts' constant. The analysis showed that most of tritium is concentrated between the first wall and the baffle, a zone which experiences high temperature gradient. The spike velocities near the FW and the SPs, along with the recirculation patterns, increase the tritium permeation towards the water pipes. In particular, the highest HTO concentration is found in the pipes near the first wall. Concerning the inventories, Aiello's correlation is more conservative since tends to overestimate the tritium retention (9.37 mg against 2.72 mg with Aiello), both in terms of inventories and in terms of permeation fluxes to the coolant. It was shown that the permeation flux to the water exhibits a maximum, and tends to decrease up to an asymptotic value. This behavior will be analyzed in detail in future works. The partial pressure inside the lithium-lead was evaluated at the lithium-lead outlet pipe and it was equal to 617 Pa with Reiter's correlation and 2.80 Pa with Aiello's correlation.

Future research might explore other geometrical configurations, due to the pre-conceptual design phase of the WCLL breeding blanket. This will have an impact on the neutronics calculations, as well as on the MHD analysis and as a consequence on tritium transport. Moreover, a pulsed-operation study for DEMO could also be conducted taking into account a more realistic assessment of the machine.

References

[1]   F. Cismondi *et al.*, "Progress of the conceptual design of the European DEMO breeding blanket, tritium extraction and coolant purification systems," *Fusion Eng. Des.*, vol. 157, no. March, p. 111640, 2020, doi: 10.1016/j.fusengdes.2020.111640.

[2]   A. Del Nevo *et al.*, "Recent progress in developing a feasible and integrated conceptual design of the WCLL BB in EUROfusion project," *Fusion Eng. Des.*, vol. 146, no. March, pp. 1805–1809, 2019, doi: 10.1016/j.fusengdes.2019.03.040.

[3]   A. Santucci *et al.*, "The issue of Tritium in DEMO coolant and mitigation strategies," *Fusion Eng. Des.*, vol. 158, no. May, p. 111759, 2020, doi: 10.1016/j.fusengdes.2020.111759.

[4]   I. Ricapito *et al.*, "Tritium technologies and transport modelling : main outcomes from the European TBM Project," *Fusion Eng. Des.*, vol. 136, pp. 128–134, 2018, doi: 10.1016/j.fusengdes.2018.01.023.

[5]   Y. Yan, A. Ying, and M. Abdou, "Numerical study of magneto-convection flows in a complex prototypical liquid-metal fusion blanket geometry," *Fusion Eng. Des.*, vol. 159, no. March, p. 111688, 2020, doi: 10.1016/j.fusengdes.2020.111688.

[6]   "COMSOL Multiphisics," 2020. http://www.comsol.com/ (accessed Sep. 01, 2020).

[7]   Los Alamos National Laboratory, "X-5 Monte Carlo Team: MCNP - A General Monte Carlo N-Particle Transport Code." Los Alamos, New Mexico, USA, 2003.

[8]   "JEFF3.3 nuclear data library." http://www.oecd-nea.org/dbdata/jeff/jeff33/#neutron. (accessed Sep. 01, 2020).

[9]   T. Hutton, J. C. Sublet, L. Morgan, and T. W. Leadbeater, "Nuclear data for fusion : Validation of typical pre-processing methods for radiation transport calculations," *Fusion Eng. Des.*, vol. 100, pp. 81–86, 2015, doi: 10.1016/j.fusengdes.2015.04.045.

[10]   F. Moro *et al.*, "Nuclear analysis of the Water cooled lithium lead DEMO reactor," *Fusion Eng. Des.*, vol. 160, no. June, p. 111833, 2020, doi: 10.1016/j.fusengdes.2020.111833.

[11]   P. J. Roache, K. N. Ghia, and F. M. White, "Editorial Policy Statement on the Control of Numerical Accuracy," *ASME J. Fluids Eng.*, vol. 108, no. 1, p. 2, 1986.

[12]   I. B. Celik, U. Ghia, P. J. Roache, C. J. Freitas, H. Coleman, and P. E. Raad, "Procedure for estimation and reporting of uncertainty due to discretization in CFD applications," *J. Fluids Eng. Trans. ASME*, vol. 130, no. 7, pp. 0780011–0780014, 2008, doi: 10.1115/1.2960953.

[13]   M. Casey and T. Wintergerste, *Industrial Computational Fluid Dynamics of Single-Phase Flows*. ERCOFTAC Best Practice Guidelines, 2000.

[14]   L. Candido, R. Testoni, M. Utili, and M. Zucchetti, "Tritium transport model at breeder unit level for WCLL breeding blanket," *Fusion Eng. Des.*, vol. 146, pp. 1207–1210, Sep. 2019, doi: 10.1016/j.fusengdes.2019.02.041.

[15]   W. M. Jones, "Thermodynamic Functions for Tritium and Tritium Hydride. The Equilibrium of Tritium and Hydrogen with Tritium Hydride. The Dissociation of Tritium and Tritium

Hydride," *J. Chem. Phys.*, vol. 16, no. 11, pp. 1077–1081, 1948.

[16] J. F. Black and H. S. Taylor, "Equilibrium in Hydrogen-Water Systems Containing Tritium," *J. Chem. Phys.*, vol. 11, no. 9, pp. 395–402, 1943.

[17] S. Eisenträger, E. Atroshchenko, and R. Makvandi, "On the condition number of high order finite element methods : Influence of p -refinement and mesh distortion," *Comput. Math. with Appl.*, vol. 80, no. 11, pp. 2289–2339, 2020, doi: 10.1016/j.camwa.2020.05.012.

[18] L. Branets and G. F. Carey, "Condition number bounds and mesh quality," *Numer. Linear Algebr. with Appl.*, vol. 17, no. 5, pp. 855–869, 2010, doi: 10.1002/nla.758.

[19] C. Bachmann *et al.*, "Overview over DEMO design integration challenges and their impact on component design concepts," *Fusion Eng. Des.*, vol. 136, no. January, pp. 87–95, 2018, doi: 10.1016/j.fusengdes.2017.12.040.

[20] F. Moro *et al.*, "Neutronic analyses in support of the WCLL DEMO design development," *Fusion Eng. Des.*, vol. 136, no. May, pp. 1260–1264, 2018, doi: 10.1016/j.fusengdes.2018.04.113.

[21] C. Alberghi, L. Candido, R. Testoni, M. Utili, and M. Zucchetti, "Magneto-convective effect on tritium transport at breeder unit level for the WCLL breeding blanket of DEMO," *Fusion Eng. Des.*, vol. 160, no. September, p. 111996, 2020, doi: 10.1016/j.fusengdes.2020.111996.

[22] F. W. Dittus and L. M. K. Boelter, "Heat transfer in automobile radiators of the tubular type," *Int. Commun. Heat Mass Transf.*, vol. 12, no. 1, pp. 3–22, 1985.

[23] D. Martelli, A. Venturini, and M. Utili, "Literature review of lead-lithium thermophysical properties," *Fusion Eng. Des.*, vol. 138, no. November 2018, pp. 183–195, 2019, doi: 10.1016/j.fusengdes.2018.11.028.

[24] F. Gillemot, E. Gaganidze, and I. Szenthe, "Material Property Handbook pilot project on EUROFER97," Final report on Deliverable no. EDDI-1.2.1-D2, 2017.

[25] F. Reiter, "Solubility and Diffusivity of Hydrogen Isotopes in Liquid Pb-15.7Li," *Fusion Eng. Des.*, vol. 14, pp. 207–211, 1991.

[26] A. Aiello, A. Ciampichetti, and G. Benamati, "Determination of hydrogen solubility in lead lithium using SOLE device," *Fusion Eng. Des.*, vol. 81, pp. 639–644, 2006.

[27] G. A. Esteban, A. Peña, I. Urra, F. Legarda, and B. Riccardi, "Hydrogen transport and trapping in EUROFER'97," *J. Nucl. Mater.*, vol. 367-370 A, no. SPEC. ISS., pp. 473–477, 2007, doi: 10.1016/j.jnucmat.2007.03.114.

[28] G. A. Esteban, A. Perujo, L. A. Sedano, and B. Mancinelli, "The surface rate constants of deuterium in the reduced activating martensitic steel OPTIFER-IVb," *J. Nucl. Mater.*, vol. 282, no. 2–3, pp. 89–96, 2000, doi: 10.1016/S0022-3115(00)00485-2.

[29] F. R. Urgorri, C. Moreno, E. Carella, J. Castellanos, A. Del Nevo, and Á. Ibarra, "Preliminary system modeling for the EUROfusion water cooled lithium lead blanket," *Fusion Sci. Technol.*, vol. 71, no. 3, pp. 444–449, 2017, doi: 10.1080/15361055.2016.1273712.

[30] E. Carella, C. Moreno, F. R. Urgorri, D. Rapisarda, and A. Ibarra, "Tritium modelling in HCPB breeder blanket at a system level," *Fusion Eng. Des.*, vol. 124, pp. 687–691, 2017, doi: 10.1016/j.fusengdes.2017.01.051.

[31] C. Mistrangelo and L. Buhler, *Magnetoconvection in HCLL Blankets*. Karlsruhe: KIT Scientific Publishing, Karlsruhe, 2014.

[32] A. Tassone, G. Caruso, F. Giannetti, and A. Del Nevo, "MHD mixed convection flow in the WCLL: Heat transfer analysis and cooling system optimization," *Fusion Eng. Des.*, vol. 146, no. March, pp. 809–813, 2019, doi: 10.1016/j.fusengdes.2019.01.087.

[33] U. Muller and L. Buhler, "Magnetofluiddynamics in channel and container." Springer, 2001.

[34] L. Candido, R. Testoni, M. Utili, and M. Zucchetti, "Tritium transport model at the minimal functional unit level for HCLL and WCLL breeding blankets of DEMO," *Fusion Eng. Des.*, 2018, doi: 10.1016/j.fusengdes.2018.05.002.

[35] C. Mistrangelo and L. Bühler, "Electro-magnetic flow coupling for liquid metal blanket applications," *Fusion Eng. Des.*, vol. 109–111, pp. 1452–1457, Nov. 2016, doi: 10.1016/j.fusengdes.2015.11.052.

[36] C. Mistrangelo and L. Bühler, "Electric flow coupling in the HCLL blanket concept," *Fusion Eng. Des.*, vol. 83, no. 7–9, pp. 1232–1237, Dec. 2008, doi: 10.1016/j.fusengdes.2008.07.004.

[37] F. Waelbroeck, P. Wienhold, J. Winter, and T. Banno, "Influence of bulk and surface phenomena on the hydrogen permeation through metals," Kernforschungsanlage Jülich GmbH, Zentralbiliothek, Verlag, Jülich, 1984.